MOA-2016-BLG-227Lb: A Massive Planet Characterized by Combining Lightcurve Analysis and Keck AO Imaging

N. Koshimoto[1,M], Y. Shvartzvald[2,K,W,U,a], D. P. Bennett[3,4,M], M. T. Penny[5,C,b], M. Hundertmark[6,7,V], I. A. Bond[8,M], W. C. Zang[9,10,C], C. B. Henderson[2,K,U,a], D. Suzuki[3,4,M], N. J. Rattenbury[11,M], T. Sumi[1,M]

and

F. Abe[12], Y. Asakura[12], A. Bhattacharya[3,4], A. Fukui[13], Y. Hirao[1], Y. Itow[12], M.C.A. Li[11], C.H. Ling[8], K. Masuda[12], Y. Matsubara[12], T. Matsuo[1], Y. Muraki[12], M. Nagakane[1], K. Ohnishi[14], C. Ranc[3,a], To. Saito[15], A. Sharan[11], H. Shibai[1], D.J. Sullivan[16], P.J. Tristram[17], A. Yonehara[18]
(MOA Collaboration)

C. R. Gelino[19,20], C. Beichman[19], J.-P. Beaulieu[21,22], J.-B. Marquette[21], V. Batista[21]
(Keck Team)

M. Friedmann[23], N. Hallakoun[23,24], S. Kaspi[23], D. Maoz[23]
(Wise Group)

G. Bryden[2], S. Calchi Novati[25,26], S. B. Howell[27]
(UKIRT Team)

T. S. Wang[9], S. Mao[9,28,29], P. Fouqué[30,31]
(CFHT-K2C9 Microlensing Survey)

H. Korhonen[32], U. G. Jørgensen[7], R. Street[33], Y. Tsapras[33,34], M. Dominik[35], E. Kerins[36], A. Cassan[37], C. Snodgrass[38], E. Bachelet[33], V. Bozza[26,39,40], D. M. Bramich[41]
(VST-K2C9 Team)

[1]Department of Earth and Space Science, Graduate School of Science, Osaka University, 1-1 Machikaneyama, Toyonaka, Osaka 560-0043, Japan

[2]Jet Propulsion Laboratory, California Institute of Technology, 4800 Oak Grove Drive, Pasadena, CA 91109, USA

[3]Laboratory for Exoplanets and Stellar Astrophysics, NASA/Goddard Space Flight Center, Greenbelt, MD 20771, USA

[4]Department of Physics, University of Notre Dame, Notre Dame, IN 46556, USA

[5]Department of Astronomy, The Ohio State University, 140 W. 18th Avenue, Columbus, OH 43210, USA

[6]Astronomisches Rechen-Institut, Zentrum für Astronomie der Universität Heidelberg (ZAH), 69120 Heidelberg, Germany

[7]Niels Bohr Institute & Centre for Star and Planet Formation, University of Copenhagen Øster Voldgade 5, 1350 - Copenhagen, Denmark

[8]Institute of Information and Mathematical Sciences, Massey University, Private Bag 102-904, North Shore Mail Centre, Auckland, New Zealand

[9]Physics Department and Tsinghua Centre for Astrophysics, Tsinghua University, Beijing 100084, China

[10]Department of Physics, Zhejiang University, Hangzhou, 310058, China

[11]Department of Physics, University of Auckland, Private Bag 92019, Auckland, New Zealand

[12]Institute for Space-Earth Environmental Research, Nagoya University, Nagoya 464-8601, Japan

[13]Okayama Astrophysical Observatory, National Astronomical Observatory, 3037-5 Honjo, Kamogata, Asakuchi, Okayama 719-0232, Japan

[14]Nagano National College of Technology, Nagano 381-8550, Japan

[15]Tokyo Metropolitan College of Industrial Technology, Tokyo 116-8523, Japan

[16]School of Chemical and Physical Sciences, Victoria University, Wellington, New Zealand

[17]University of Canterbury Mt John Observatory, P.O. Box 56, Lake Tekapo 8770, New Zealand

[18]Department of Physics, Faculty of Science, Kyoto Sangyo University, Kyoto 603-8555, Japan

[19]NASA Exoplanet Science Institute, California Institute of Technology, Pasadena, CA 91125, USA

[20]Infrared Processing and Analysis Center and NASA Exoplanet Science Institute, California Institute of Technology, Pasadena, CA 91125, USA

[21]UPMC-CNRS, UMR 7095, Institut dAstrophysique de Paris, 98Bis Boulevard Arago, F-75014 Paris, France

[22]School of Physical Sciences, University of Tasmania, Private Bag 37 Hobart, Tasmania 7001 Australia

[23]School of Physics and Astronomy and Wise Observatory, Tel-Aviv University, Tel-Aviv 69978, Israel

[24]European Southern Observatory, Karl-Schwarzschild-Straße 2, D-85748 Garching, Germany

[25]IPAC, Mail Code 100-22, Caltech, 1200 E. California Blvd., Pasadena, CA 91125

[26]Dipartimento di Fisica "E. R. Caianiello", Università di Salerno, Via Giovanni Paolo II, 84084 Fisciano (SA), Italy

[27]Kepler & K2 Missions, NASA Ames Research Center, PO Box 1,M/S 244-30, Moffett Field, CA 94035

[28]National Astronomical Observatories, Chinese Academy of Sciences, A20 Datun Rd., Chaoyang District, Beijing 100012, China

[29]Jodrell Bank Centre for Astrophysics, Alan Turing Building, University of Manchester, Manchester M13 9PL, UK

[30]CFHT Corporation, 65-1238 Mamalahoa Hwy, Kamuela, Hawaii 96743, USA

[31]Université de Toulouse, UPS-OMP, IRAP, Toulouse, France

[32]Dark Cosmology Centre, Niels Bohr Institute, University of Copenhagen, Juliane Maries Vej 30, 2100 - Copenhagen Ø, Denmark

[33]Las Cumbres Observatory Global Telescope Network, Inc., 6740 Cortona Drive, Suite 102, Goleta, CA 93117, USA

[34]Astronomisches Rechen-Institut, Zentrum für Astronomie der Universität, Heidelberg, Mönchhofstr. 12-14, 69120 Heidelberg, Germany

[35]SUPA, School of Physics & Astronomy, University of St Andrews, North Haugh, St Andrews KY16 9SS, UK

[36]Jodrell Bank Centre for Astrophysics, School of Physics and Astronomy, University of Manchester, Oxford Road, Manchester M13 9PL, UK

[37]Sorbonne Universités, UPMC Univ Paris 6 et CNRS, UMR 7095, Institut dAstrophysique de Paris, 98 bis bd Arago, 75014 Paris, France

[38]Planetary and Space Sciences, Department of Physical Sciences, The Open University, Milton Keynes, MK7 6AA, UK

[39]Istituto Internazionale per gli Alti Studi Scientifici (IIASS), Via G. Pellegrino 19, 84019 Vietri sul Mare (SA), Italy

[40]INAF - Observatory of Capodimonte, Salita Moiariello, 16, 80131, Naples, Italy

[41]Qatar Environment and Energy Research Institute(QEERI), HBKU, Qatar Foundation, Doha, Qatar

[M]MOA Collaboration

[K]Keck team

[W]Wise group

[U]UKIRT team

[C]CFHT-K2C9 Microlensing Survey

[V]VST-K2C9 Team

ABSTRACT

We report the discovery of a microlensing planet — MOA-2016-BLG-227Lb — with a massive planet/host mass ratio of $q \simeq 9 \times 10^{-3}$. This event was fortunately observed by several telescopes as the event location was very close to the area of the sky surveyed by Campaign 9 of the *K2* Mission. Consequently, the planetary deviation is well covered and allows a full characterization of the lensing system. High angular resolution images by the Keck telescope show excess flux other than the source flux at the target position, and this excess flux could originate from the lens star. We combined the excess flux and the observed angular Einstein radius in a Bayesian analysis which considers various possible origins of the measured excess flux as priors, in addition to a standard Galactic model. Our analysis indicates that it is unlikely that a large fraction of the excess flux comes from the lens. We compare the results of the Bayesian analysis using different priors for the probability of hosting planets with respect to host mass and find the planet is likely a gas-giant around an M/K dwarf likely located in the Galactic bulge. This is the first application of a Bayesian analysis considering several different contamination scenarios for a newly discovered event. Our approach for considering different contamination scenarios is crucial for all microlensing events which have evidence for excess flux irrespective of the quality of observation conditions, such as seeing, for example.

Subject headings: gravitational lensing, planetary systems

1. Introduction

Gravitational microlensing is a powerful method for detecting extrasolar planets (Mao & Paczynski 1991; Gould & Loeb 1992; Gaudi 2012). Compared to other detection techniques, microlensing is sensitive to low-mass planets (Bennett & Rhie 1996) orbiting beyond the snow line around relatively faint host stars like M dwarfs or brown dwarfs (Bennett et al. 2008; Sumi et al. 2016), which is complementary to other methods.

A difficulty with the microlensing method is the determination of the mass of a lens M_L and the distance to the lens system D_L. If we have an estimate for the angular Einstein

[a]NASA Postdoctoral Program Fellow

[b]Sagan Fellow

radius θ_E and the microlens parallax π_E, the mass is directly determined by

$$M_L = \frac{\theta_{\rm E}}{\kappa \pi_{\rm E}} \ , \tag{1}$$

where $\kappa = 8.144$ mas $M_\odot^{-1}$ (Gould 1992; Gaudi et al. 2008; Muraki et al. 2011). Because the relative parallax $\pi_{\rm rel} \equiv {\rm AU}(1/D_L - 1/D_S)$ is derived from $\pi_E = \pi_{\rm rel}/\theta_E$, we can also calculate the distance D_L, where we assume the distance to the source D_S is at the Galactic centre, $D_S \simeq 8$ kpc. However the microlens parallax can be observed only in relatively rare events while the angular Einstein radius is commonly observed for planetary events.

One strategy for events in which the microlens parallax cannot be detected is to estimate the probability distribution of the lens mass by a Bayesian analysis using a standard Galactic model as the prior probability distribution (e.g., Beaulieu et al. 2006; Bennett et al. 2014; Koshimoto et al. 2014; Shvartzvald et al. 2014). However this Galactic model includes no information on the distribution of planets. It may be that the probability of hosting a planet of the measured mass ratio and separation depends on the host mass or the distance from the Galactic center. But, without mass and distance measurements, these quantities are determined by our Bayesian prior assumptions. As a case in point, Bennett et al. (2014) analyzed MOA-2011-BLG-262 and found a planetary mass host orbited by an Earth-mass "moon" model had almost the same likelihood as a star+planet model. But, since we have no precedent for such a rogue planet+moon system, they selected the more conventional star+planet system as the favored model. Also, the first discovered microlensing planet, OGLE-2003-BLG-235Lb, was at first thought to be a giant planet around an M dwarf with a mass of $M_* \sim 0.36 M_\odot$ from a Bayesian analysis (Bond et al. 2004). Such a system is predicted to be rare according to the core accretion theory of planet formation (Laughlin et al. 2004; Kennedy & Kenyon 2008). However the system was revealed to be a giant planet around a more massive host star with mass of $M_* = 0.63^{+0.07}_{-0.09} M_\odot$ by combining the Hubble Space Telescope (*HST*) observations and analyzing light assumed to come from the lens star (Bennett et al. 2006).

If we can measure the apparent magnitude of the lens flux by high angular resolution imaging with adaptive optics (AO) or *HST* (e.g., Bennett et al. 2006, 2007, 2015; Batista et al. 2015), we can then calculate the lens mass M_L by using the mass-distance relation determined by the light curve measurement of $\theta_{\rm E}$ with a mass-luminosity relation to convert the measured lens flux into a mass, M_L, and distance, D_L, for the lens system. The reason why we need high resolution imaging to do that is because the source stars are located in very crowded Galactic bulge fields and the seeing effects for ordinary ground-based image imply that most images of source stars include blended flux from unrelated nearby stars.

Because the size of the angular Einstein radius is $\lesssim 1$ mas, and the lens-source rela-

tive proper motion is typically $\mu_{\rm rel} \sim 6\,{\rm mas/yr}$, it is possible that the lens and source stars will remain unresolved in high angular resolution images taken within a few years of the microlensing event. In such cases, there will be excess flux above that contributed by the source star and this excess flux must include the lens star flux. Some studies (Batista et al. 2014; Fukui et al. 2015; Koshimoto et al. 2017b), which detected an excess flux, have assumed that this excess flux is dominated by the lens flux, and they have derived the lens mass under this assumption.

With this method, it would seem that no assumptions are required regarding the probability of the microlens stars to host planets, and there would be no biases due to any inadequacies of the Galactic model used. However, in another paper Koshimoto et al. (2017a), we consider the possibility of contamination of these excess flux measurements by unrelated stars and companions to the source and lens stars using a Bayesian method. We find that it can be difficult to exclude all these contamination scenarios, especially for events with relatively small angular Einstein radii. In those cases where we cannot exclude the contamination scenarios, we can again use a Bayesian analysis similar to the one described above to estimate the probability distribution of the lens properties. This means that we need to assume prior distributions for stellar binary systems and the stellar luminosity function even when we have detected excess flux in high angular resolution images. In cases where the lens properties are confirmed by a measurement of the lens-source relative proper motion (Bennett et al. 2015; Batista et al. 2015) or microlensing parallax measurements (Gaudi et al. 2008; Beaulieu et al. 2016; Bennett et al. 2016), this contamination can be ruled out. Attempts at lens-source relative proper motion measurements can also confirm contamination (Bhattacharya et al. 2017) in cases where the measured proper motion of the star responsible for the excess flux does not match the microlensing light curve prediction.

This paper reports the discovery and our analysis of the microlensing planetary event MOA-2016-BLG-227, which was observed by the Keck telescope using adaptive optics after the end of the event. Our observations and data reduction to light curve photometry are described in Sections 2 and 3. Our modeling results are presented in Sections 4. In Section 5, we model the foreground extinction by comparing observed color magnitude diagrams (CMDs) to different extinction laws and compare the results from the different extinction laws. Then, we use the favored extinction law to determine the angular Einstein radius, $\theta_{\rm E}$. Section 6 describes our observations and the photometry for the Keck AO images, and we extract the consequent excess flux. In Section 7, we describe the Bayesian analysis we used to include estimates of contamination probabilities and the results of the posterior probability density distribution of the lens properties are presented. Finally, we discuss and conclude the results of our work in Section 8.

2. Observations

The Microlensing Observations in Astrophysics (MOA; Bond et al. 2001, Sumi et al. 2003) group continues to conduct a high cadence survey towards the Galactic bulge using the 2.2-deg^2 FOV MOA-cam3 (Sako et al. 2008) CCD camera mounted on the 1.8 m MOA-II telescope at the University of Canterbury Mt. John Observatory in New Zealand. The MOA group alerts about 600 microlensing events per year. Most of the observations are conducted through the custom MOA-Red filter which is similar to the sum of the standard Cousins R- and I-band filters, while observations with the MOA V filter (Bessell V-band) are conducted once every clear night.

The microlensing event MOA-2016-BLG-227 was discovered at (R.A., Dec.)$_{J2000}$ = (18:05:53.70, -27:42:51.43) or $(l, b) = (3.303°, -3.240°)$ by MOA on 5 May 2016 (HJD$' \equiv$ HJD - 2450000 $\sim$ 7514). This event occurred during the microlensing Campaign 9 of the *K2* Mission (Henderson et al. 2016) and it was located close to (but not in) the area of sky that was surveyed for the *K2* microlensing of Campaign 9. This part of the *K2* field that was downloaded at 30 minute intervals is known as the "superstamp." Because this event was so close to the superstamp, several other groups also observed this event.

The Wise group used the Jay Baum Rich 0.71m Telescope (C28) at the Wise Observatory in Israel, which is equipped with a 1 deg^2 camera, to monitor the *K2*C9 superstamp during the campaign. Six survey fields were observed 3–5 times per night with the Astrodon Exo-Planet BB (blue-blocking) filter. Although the MOA-2016-BLG-227 target was just outside the *K2*C9 superstamp, it was still within the Wise survey footprint.

The event was also observed with the wide-field near infrared (NIR) camera (WFCAM) on the UKIRT 3.8m telescope on Mauna Kea, Hawaii, as part of a NIR microlensing survey in conjunction with the *K2*C9 (Shvartzvald et al. 2017) survey. The UKIRT survey covered 6 deg^2, including the entire *K2*C9 superstamp and extending almost to the Galactic plane, with a cadence of 2–3 observations per night. Observations were taken in H-band, with each epoch composed of sixteen 5-second co-added dithered exposures (2 co-adds, 2 jitter points, and 2×2 microsteps).

The Canada France Hawaii Telescope (CFHT), also on Mauna Kea, serendipitously captured data on the event during the CFHT-*K2*C9 Microlensing Survey. The CFHT operated a multi-color survey of the *K2* Campaign 9 superstamp using the Megacam Instrument (Boulade et al. 2003). The CFHT observations for the event were conducted through the g-, r- and i-band filters.

The VLT Survey Telescope (VST) is a 2.61m telescope installed at ESO's Paranal Observatory that is dedicated to optical surveys. For the observing period 97A proposals

were carried out as a 99-hours filler program. The telescope was available when the seeing was worse than 1 arcsec or conditions were non-photometric. As a consequence, observations were carried out whenever the seeing was worse than 1 arcsec or conditions were non-photometric. The main objective of the microlensing program was to monitor the superstamp of the *K2* campaign 9 in an automatic survey for improving the event coverage and securing color-information in SDSS r and Johnson V passbands. Due to weather conditions, Johnson V images were only taken in the second half of the *K2*C9 survey, and therefore MOA-2016-BLG-227 is only covered by SDSS r. The exact pointing strategy was adjusted to cover the superstamp with 6 pointings and to contain as many microlensing events from earlier seasons as possible. In addition, a two-point dither was requested to reduce the impact of bad pixels and detector gaps. Consequently, some events, like MOA-2016-BLG-227, received more coverage and have been observed with different CCDs.

Figure 1 shows the observed light curve. MOA alerted a light curve anomaly for this event on 9 May 2016 (HJD$' \sim 7518$), and identified the anomaly as a planetary signal 4.5 hours after the anomaly alert. Although MOA detected a strong planetary caustic exit, the observing conditions before and after this caustic exit were poor at the MOA observing site both immediately before and after this strong light curve feature. Fortunately, the additional observations from the Wise, UKIRT, CFHT and VST telescopes covered the other important features of the MOA-2016-BLG-227 light curve.

3. Data Reduction

Photometry for the MOA, Wise and UKIRT data were obtained using the offline difference image analysis pipeline of Bond et al. (2017) in which stellar images are measured using an analytical PSF model of the form used in the DoPHOT photometry code (Schechter, Mateo, & Saha 1993).

Differential flux lightcurves of the CFHT data were produced from Elixir calibrated images[1] using a custom difference imaging analysis pipeline based on ISIS version 2.2 (Alard & Lupton 1998; Alard 2000) and utilizing an improved interpolation routine[2] (Siverd et al. 2012; Bertin & Arnouts 1996). Further details of the CFHT data reduction will be presented in a future paper.

Since there is no public VST instrument pipeline, calibration images from ESO's archive were used and combined. Restrictive bad pixel masks have been extracted to ensure that no

[1] `http://www.cfht.hawaii.edu/Instruments/Elixir/`

[2] `http://verdis.phy.vanderbilt.edu/`

flatfield pixels varying nightly by more than 1 % or by 10 % on the averaged flatfield have entered the analysis. The calibrated images have been reduced with the difference imaging package DanDIA (Bramich 2008) relying on the numerical kernel approach to difference image analysis and using the routines from the RoboNet reduction pipeline (Tsapras et al. 2009).

It is known that the error bars given by crowded field photometry codes can be under or overestimated depending on the specific details for each event. The error bars provided by the photometry codes are sufficient to find the best fit models, but they do not allow a proper determination of the microlensing light curve model parameter uncertainties. Therefore, we empirically normalize the errors in each data-set. We used the formula presented in Yee et al. (2012) for normalization, $\sigma_i' = k\sqrt{\sigma_i^2 + e_{\rm min}^2}$ where σ_i is the original error of the ith data point in magnitudes, and the parameters for normalization are k and $e_{\rm min}$. k and $e_{\rm min}$ are adjusted so that the cumulative χ^2 distribution as a function of the number of data points sorted by each magnification of the preliminary best-fit model is a straight line of slope 1.

Our dataset used for this analysis and the obtained normalization parameters are summarized in Table 1.

4. Modeling

Because the light curve shows clear anomalies caused by the source crossing a binary-lens caustic, we need to include terms in the binary lens model which account for the finite size of the source star. The model requires the following parameters: the time of the source closest approach to the lens center of mass, t_0, the impact parameter of the source trajectory with respect to the center of mass of the lens system u_0,the Einstein radius crossing time $t_{\rm E} = \theta_{\rm E}/\mu_{\rm rel}$, the mass ratio of two lenses $q \equiv M_{\rm p}/M_{\rm host}$ the separation of the lens masses, s, the angle between the trajectory and the binary lens axis, α, and the source size $\rho \equiv \theta_*/\theta_{\rm E}$. The parameters u_0, s, and ρ are given in units of the Einstein radius, and $M_{\rm host}$ and $M_{\rm p}$ are the masses of the host star and its planetary companion. With these seven parameters, we can calculate the magnification as a function of time $A(t)$. In the crowded stellar fields where most microlensing events, most source stars are blended with one or more other stars, so that we cannot determine the source star brightness directly from images where the source is not magnified. Therefore, we add another set of linear parameters for each data set, the source and blend fluxes, f_S and f_b, so that we can compare the model flux, $F(t) = f_S A(t) + f_b$, to the observations.

When we include the finite source effect, we have to consider the spatial variation of

the source flux due to limb-darkening. We adopt a linear limb-darkening law with one parameter, u_λ, for each data set. Considering the source intrinsic color which is discussed in Section 5.1 and the typical parameters for such kinds of star from Bensby et al. (2013), we assumed an effective temperature of $T_{\rm eff} \sim 5500$ K, a surface gravity of $\log\ g = 4.0$ cm s^{-2}, a metallicity of [M/H] = 0.0 and a microturbulence parameter of $\xi = 1.0$ km s^{-1}. We selected the limb-darkening coefficients from the ATLAS model by Claret & Bloemen (2011). Based on those assumptions, we have $u_{\rm MOA-Red} = 0.5585$ for MOA-Red, $u_V = 0.6822$ for MOA-V, $u_R = 0.6015$ for Wise Astrodon, $u_H = 0.3170$ for UKIRT H, $u_i = 0.5360$ for CFHT i, $u_r = 0.6257$ for CFHT r, VST-71 r and VST-95 r, and $u_g = 0.7565$ for CFHT g. We have used the mean of the u_I and u_R values for the limb-darkening coefficients for the MOA-Red passband. Here we have adopted the R-band limb-darkening coefficient for the Wise Astrodon data. As the Wise Astrodon filter is non-standard, our choice is not perfect. However we note that even if we adopt $u = 0$ for the limb darkening coefficient used with the Wise data, our χ^2 value changes by only 1.5. The limb-darkening coefficients we used are also shown in Table 1.

To find the best-fit model, we conducted the global grid search method described in Sumi et al. (2016) where we fit the light curves using a Markov Chain Monte Carlo (MCMC) approach (Verde et al. 2003), with magnification calculations from the image centered ray-shooting method (Bennett & Rhie 1996; Bennett 2010). As a result, we found a unique best-fit model in which the source crosses the resonant caustic. We show the model light curve in Figure 1, the caustic and the source trajectory in Figure 2 and the best-fit model parameters in Table 2.

Additionally, we tried to fit the light curve including the microlensing parallax effect due to the Earth's orbital motion (Gould 1992; Alcock et al. 1995) although this event is unlikely to reveal a significant microlensing parallax signal because of its relatively short timescale. We found the best-fit parallax model produced a formally better fit compared to the best-fit non-parallax model above by $\Delta\chi^2 \sim 14$. However, the parts of the lightcurve which contributed to this decrease in χ^2 have a scatter similar to the variability of the baseline MOA data, and the best fit microlensing parallax parameter were unlikely large, $\pi_E = 1.3^{+2.1}_{-0.3}$, leading very small lens mass of $M_L \sim 0.02 M_\odot$. Therefore we conclude that the smaller χ^2 of the parallax model was due to some small systematic error in the MOA light curve.

5. Angular Einstein Radius

Because we have measured the finite source size, ρ, to a precision of $\sim 2\,\%$, the determination of the angular source star radius θ_* will yield the angular Einstein radius $\theta_E = \theta_*/\rho$. This, in turn, provides the mass-distance relation, (Bennett 2008; Gaudi 2012)

$$M_L = \frac{c^2}{4G}\theta_E^2 \frac{D_S D_L}{D_S - D_L} = 0.9823\, M_\odot \left(\frac{\theta_E}{1\,\mathrm{mas}}\right)^2 \left(\frac{x}{1-x}\right)\left(\frac{D_S}{8\,\mathrm{kpc}}\right) \ , \tag{2}$$

where $x = D_L/D_S$. We can empirically derive θ_* from the intrinsic source magnitude and the color (Kervella et al. 2004; Boyajian et al. 2014).

5.1. Calibration

Our fist step is to calibrate the source magnitude to a standard photometric system. We cross referenced stars in the event field between our DoPHOT photometry catalog of stars in the MOA image and the OGLE-III catalog (Szymański et al. 2011) to convert MOA-Red and MOA V into standard magnitudes. Following the procedure presented by Bond et al. (2017), we had

$$I_{\mathrm{OGLE-III}} - R_{\mathrm{MOA}} = (28.186 \pm 0.006) - (0.247 \pm 0.005)(V-R)_{\mathrm{MOA}} \tag{3}$$

$$V_{\mathrm{OGLE-III}} - V_{\mathrm{MOA}} = (28.391 \pm 0.004) - (0.123 \pm 0.004)(V-R)_{\mathrm{MOA}}. \tag{4}$$

Using these calibration formulae and the result of lightcurve modeling, we obtained the source standard magnitude $I_S = 19.536 \pm 0.019$ and the color $(V-I)_S = 1.60 \pm 0.03$.

We follow a similar procedure to cross referenced stars in our DoPHOT photometry catalog of stars in the UKIRT images to stars in the VVV (Minniti et al. 2010) catalog which is calibrated to the Two Micron All Sky Survey (2MASS) photometric system (Carpenter 2001), thereby obtaining the relationship between these photometric systems. We used this same VVV catalog to plot CMDs in the next section and for the analysis of the Keck images in Section 6. Using the UKIRT H source magnitude obtained from the light curve modeling and our derived conversion, we get $H_S = 17.806 \pm 0.017$. We also obtained colors for the source star: $(V-H)_S = 3.33 \pm 0.03$ and $(I-H)_S = 1.730 \pm 0.017$.

5.2. Extinction and the angular Einstein radius

Next, we correct for extinction following the standard procedure (Yoo et al. 2004; Bennett et al. 2010) using red clump giants (RCGs) as standard candles.

5.2.1. Measured RCGs centroid

Figure 3 shows the $(V-I,I)$ and $(V-H,H)$ color-magnitude diagrams (CMDs) for stars within 2 arcmin of the source star. The V and I magnitudes are taken from the OGLE-III photometry catalog (Szymański et al. 2011), and the VVV (Minniti et al. 2010) catalog to the 2MASS photometry scale for H magnitudes. To plot the $V-H$ vs H CMD, we cross referenced stars in the VVV catalog to stars in the OGLE-III catalog. Note that we used only isolated stars cross-matched to within 1 arcsec of stars in the OGLE-III catalog to avoid contamination of blended stars, and this value of 1 arcsec corresponds to the average seeing in the VVV images. We found the centroid of RCGs in each of the CMDs, including $I-H$ vs H CMD, which is not shown, as follows: $I_{\rm cl} = 15.33 \pm 0.05$, $(V-I)_{\rm cl} = 1.88 \pm 0.02$, $(V-H)_{\rm cl} = 4.03 \pm 0.06$ and $(I-H)_{\rm cl} = 2.11 \pm 0.03$.

5.2.2. Intrinsic magnitude and color of RCG

We use $(V-I)_{\rm cl,0} = 1.06 \pm 0.03$ and $I_{\rm cl,0} = 14.36 \pm 0.05$ for the intrinsic $V-I$ color and I magnitude of the RCGs (Bensby et al. 2013; Nataf et al. 2016). Following Nataf et al. (2016), we calculated the intrinsic color of $V-H$ and $I-H$ in the photometric system we are using now (i.e., Johnson V, Cousins I and 2MASS H) by the tool provided by Casagrande & VandenBerg (2014) which is based on a grid of MARCS model atmospheres (Gustafsson et al. 2008). Assuming the atmospheric parameters [Fe/H] $= -0.07 \pm 0.10$ (Gonzalez et al. 2013), $\log\ g = 2.3 \pm 0.1$ and $[\alpha/{\rm Fe}] = 0.20 \pm 0.05$ (Hill et al. 2011; Johnson et al. 2014) for the RCGs in the event field, we derived $(V-H)_{\rm cl,0} = 2.36 \pm 0.09$ and $(I-H)_{\rm cl,0} = 1.30 \pm 0.06$ by adjusting the last atmospheric parameter $T_{\rm eff}$ so that the $(V-I)$ value takes between $1.03 < (V-I) < 1.09$. We summarize the magnitude and colors for RCGs and the source in Table 3.

5.2.3. Angular Einstein radius

By subtracting the intrinsic RCG color and magnitude values from the measured RCG positions in our CMDs, we obtained the observed value, $A_{I,{\rm obs}} = 0.98 \pm 0.07$, and color excess values of $E(V-I)_{\rm obs} = 0.82 \pm 0.04$, $E(V-H)_{\rm obs} = 1.67 \pm 0.11$ and $E(I-H)_{\rm obs} = 0.81 \pm 0.07$. Following the method by Bennett et al. (2010), we fitted these values to the extinction laws of Cardelli et al. (1989), Nishiyama et al. (2009) and Nishiyama et al. (2008) separately and compared the results. We present this analysis in Section A in the appendix. As a result of the analysis, we decided to adopt the results from the Nishiyama et al. (2008) extinction laws

for the following analysis, which gives us the extinction value in $H-$band $A_H = 0.19 \pm 0.02$ and the angular source radius $\theta_* = 0.68 \pm 0.02$ μas. With the θ_* value, we determine the angular Einstein radius to be $\theta_E = \theta_*/\rho = 0.227^{+0.006}_{-0.009}$ mas, and this implies that the lens-source relative proper motion is $\mu_{\rm rel} = \theta_E/t_E = 4.88^{+0.14}_{-0.17}$ mas/yr.

6. Excess Flux from Keck AO Images

On August 13, 2016 (HJD$'$ = 7613.85) we observed MOA-2016-BLG-227 using NIRC2 behind the LGS AO system on the Keck II telescope on Mauna Kea, Hawaii. Observations were taken in the H-band using the wide-field camera (0.04"/pix). We took four dithered frames with 5 sec exposures and an additional three dithered frames with a total integration time of 90 sec (6 co-adds of 15 sec exposures). The first set allows for photometric calibration using bright stars and the second provides the increased photometric depth required for a high signal-to-noise flux measurement of the target. Standard dark and flat field corrections were applied to the images, and sky subtraction was done using a stacked image of a nearby empty field. Each set of images was then astrometrically aligned and stacked. Finally, we use SExtracor (Bertin & Arnouts 1996) to extract the Keck source catalog from the stacked images.

A calibration catalog was extracted using an H image of the target area taken by the VISTA Variables in the Via Lactea survey (VVV; Minniti et al. 2010) reprocessed following the approach described in Beaulieu et al. (2016). We apply a zero point correction for the Keck source catalog using common VVV and Keck sources. The estimated uncertainty on the zero point is 0.05. Figure 4 shows a nearby bright star to the target. As a consequence the dominant error contribution is the background estimation of the target on the Keck image.

We extract the source coordinates using a MOA difference image of the event while it was highly magnified. We then identify the position of the microlensing target (source+lens) on the Keck image (see Figure 4), and measure its brightness to be $H_{\rm Keck} = 17.63 \pm 0.06$. Due to technical problems with the AO system the corrections were not optimal, giving a sharp core but a rather sparse halo around each object. Thus, the FWHM of the Keck image is 0.184″ (measured as the average of isolated bright stars near the target), which sets a limit on our ability to exclude flux contribution from stars unrelated to the source and the lens, as we discuss further below.

We have the (extinction uncorrected) source magnitude in H-band $H_S = 17.806 \pm 0.017$ from Section 5.1 thanks to the UKIRT H light curve. Because the Keck observation time is

after the event reached the baseline ($t_{\rm obs,Keck} - t_0 = 5.7\ t_E$), we can extract the excess flux by subtracting just the source flux from the target flux, $H_{\rm ex,obs} = 19.7 \pm 0.4$.

7. Lens Properties through Bayesian Analysis

In Koshimoto et al. (2017a), we present a systematic approach to the possibility of lens detection in high-angular resolution images from an AO system or a space-based telescope, like *HST*, using a Bayesian analysis. This analysis gives us the posterior probability distributions for the lens mass and the distance by combining the results of the light curve modeling and the measured excess flux value. The method is, briefly:

1. Assume prior probability distributions of four possibilities of the origin of the excess flux. These four possibilities are the lens star, unrelated ambient stars, source companions or lens companions, and we denote their fluxes by F_L, $F_{\rm amb}$, F_{SC} and F_{LC}, respectively.

2. Pick a number of combinations of the flux values for each possible contributing star from the prior probability distributions and extract the combinations which have the total excess flux values, $F_{\rm excess} = F_L + F_{\rm amb} + F_{SC} + F_{LC}$, consistent with the observed excess flux.

The extracted combinations at step 2 corresponds to the posterior probability distributions. We conduct this calculation using the values for MOA-2016-BLG-227.

7.1. Prior probability distributions

Now, we have to determine the prior probability distributions of the four possibilities for the origin of the excess flux at the position of the source. We use all the information we have about this event — except for the value of excess flux — to create our prior probability distributions. This means that we include the FWHM of the Keck images, but not the measured magnitude of the object at the location of the microlensing event. Table 4 shows a summary of our assumptions.

7.1.1. Lens flux prior

For the lens flux prior distribution, we conducted a Bayesian analysis using the observed t_E and θ_E values and the Galactic model, which has been used in a number of previous papers (Alcock et al. 1995; Beaulieu et al. 2006) to estimate lens properties when microlensing parallax was not detected in the event. We used the Galactic model of Han & Gould (1995) for the density and the velocity models and used the mass function presented in the Supplementary Information section of Sumi et al. (2011). Using this result and the mass-luminosity relation presented in Koshimoto et al. (2017a), we obtained the prior distribution for the lens apparent magnitude, H_L. We adopt formula the extinction to the lens, $A_{H,L} = (1 - e^{-D_L/h_{\rm dust}})/(1 - e^{-D_S/h_{\rm dust}})\ A_{H,S}$, following Bennett et al. (2015), where $h_{\rm dust} = (0.1\ {\rm kpc})/\sin b$ is a scale height of the dust toward the Galactic bulge. Note that this Bayesian analysis gives us not only H_L, but also the accepted combinations of M_L, D_L and D_S which are consistent with the observed t_E and θ_E values. These values may be needed for the calculation of probability distributions below.

7.1.2. Ambient star flux prior

In order to determine the prior probability distribution for the flux of any unrelated ambient stars, we determine the number density in Keck AO image, centered on the target, within a magnitude range with high completeness and divide that number by the area of the image. Then we use the luminosity function of Zoccali et al. (2003) to derive the number density of stars as a function of H magnitude. Of course, we must correct this calculation for differences of the extinction and the distance moduli between our field and their field, using the distance moduli from Table 3 of Nataf et al. (2013) and the extinction values for both fields.

When correcting for the extinction difference, we also consider the difference between the extinction laws used. Zoccali et al. (2003) derive an A_H value using the C89 extinction law with $R_V = 3.1$, whereas our preferred N08 extinction law implies a significantly different A_H value. To correct for this difference, we calculated the A_H value towards their field using the N08 extinction law fit to the RCG centroid in the OGLE-III CMD and the R_{JKVI} value from Table 3 of Nataf et al. (2013) for their field. The A_H value we derived here is $A_H = 0.122$, which is different from the value of $A_H = 0.265$ used by Zoccali et al. (2003). Therefore, we converted their extinction corrected H-band luminosity function to a luminosity function with our preferred extinction model by adding $\Delta A_H = 0.265 - 0.122 = 0.142$ to their extinction corrected magnitudes, and then we added the extinction appropriate for our field, $A_H = 0.19$.

We assume that we can resolve an ambient star only if it is separated from the source by $\geq 0.8\,\mathrm{FWHM} = 148\,\mathrm{mas}$, so the expected number of ambient stars within the circle is derived by multiplying the area of this unresolvable region by the total number density derived above. We determine the number of stars by following the Poisson distribution with the mean value of the expected number of stars. We use the corrected luminosity function to determine the magnitude of each star.

7.1.3. Source and lens companion flux priors

We calculate the source and lens companion flux priors with the stellar binary distribution described in detail by Koshimoto et al. (2017a). This is based on the distribution summarized by Duchêne & Kraus (2013), where the binary distribution is described by distributions of multiplicity fraction, mass ratio and semi-major axis.

For the flux of source companions, we calculate the source mass $M_{SC} = q_{SC} M_S$ and then convert that into the magnitude H_{SC} using a mass-luminosity relation, where the mass ratio q_{SC} comes from the binary distribution and we estimate the source mass M_S using H_S, D_S and the mass-luminosity relation. Similarly, we calculate the lens companions magnitude H_{LC} from $M_{LC} = q_{LC} M_L$, where the lens mass M_L comes from the probability distribution of the same Bayesian analysis we conducted to get the probability distribution of the lens flux.

We consider only companions located in unresolvable regions for the probability distributions as in the case of ambient stars. The difference from the case where the excess light comes from ambient stars is that we must now exclude companions that are too close to the source and lens as well as companions that are so widely separated that they will be resolved. Companions that are too close to the source or lens could be magnified themselves or serve as an additional lens star. In principle, we could also apply this to the ambient stars, but it would have no effect, because the probability of an ambient star very close to the source or lens is much smaller than that of a companion. Following Batista et al. (2014), we adopt $\theta_E/4$ as the close limit for source companions and $w_{LC} < u_0$ as the close limit for lens companions, where w_{LC} is the size of the caustic created by the hypothetical companion to the lens, $w_{LC} = 4q_{LC}/(s_{LC} - s_{LC}^{-1})^2$ where s_{LC} is the separation between the lens and that companion. We used 0.8 FWHM as the maximum unresolvable radius.

We have also considered triple and quadruple systems when estimating the effect of companions to the source and lens, following Koshimoto et al. (2017a), but we found no significant difference from the case of only considering binary systems. We therefore don't

include triple and quadruple systems in this paper for clarity and simplicity.

7.1.4. Excess flux prior

Figure 5 shows the prior probability distributions we derived above. In addition to the magnitude of the four types of stars that might contribute to the excess flux, we show the prior distributions for the total excess flux, $H_{\rm excess}$, the lens mass, M_L, and the distance to the lens D_L. Some of the panels in this figure have total probabilities $P_{\rm total} < 1$. This is because many stars do not have binary companions and there is a large probability of no measurable flux from an ambient star. The $H_{\rm excess}$ prior indicates a high probability at the observed magnitude of $H_{\rm ex,obs} = 19.7 \pm 0.4$. The three panels for individual stars, H_L, $H_{\rm amb}$ and H_{SC} show similar probabilities at the observed excess flux value. This indicates that it will be difficult to claim that all of the excess comes from the lens itself.

7.2. Posterior probability distributions

We generate the posterior probability distributions shown in Figure 6 by extracting combinations of parameters which have values of $H_{\rm excess}$ consistent with the measured value of $H_{\rm ex,obs} = 19.7 \pm 0.4$ using a Gaussian distribution in fluxes (not magnitudes). The probability that $H_L \leq 20$ is almost same as the probability for $H_{\rm SC} \leq 20$ and slightly higher, but competitive with, the probability that $H_{\rm amb} \leq 20$, which results in very loose constraints on H_L and M_L. This result is consistent with our expectation as discussed in Section 7.1.4.

The third to sixth columns of Table 5 shows the median, the 1 σ error bars, and the 2 σ range for H_L, M_L and D_L for both the prior and posterior distributions. This same table also shows the values of the planet mass $M_{\rm p}$, the projected separation $a_\perp$ and the three-dimensional star-planet separation a_{3d} calculated from the probability distributions, where a_{3d} is statistically estimated assuming a uniform orientation for the detected planets. In the bottom three rows, we present the probabilities that the fraction of the excess flux due to the lens, f_L is larger than 0.1, 0.5 and 0.9, which correspond to magnitude difference between the lens and the total flux excess of 2.5 mag, 0.75 mag and 0.11 mag.

The posteriors distributions for the lens system properties are remarkably similar to the prior distributions. When we only look at the 1σ range of the prior and posterior distributions, we see that the lens system likely consists of an M or K dwarf star host and a gas-giant planet. However the prior and posterior distributions differ from each other when we consider the 2σ ranges and the tails of the distributions. The possibility of a G dwarf host

star is ruled out by the posterior distribution while the host star can be a G dwarf according to the prior distribution, which means we can claim that the host star is very likely an M or K dwarf with more confidence thanks to the excess flux information.

7.3. Comparison of different planetary host priors

There is one prior that we have implicitly assumed so far is that has a significant influence on our results, although we have little data to constrain the correct functional form of this prior. MOA-2016-BLG-227 is unlike most microlensing events in that the light curve has revealed a planetary mass companion to the lens star. We have assumed that this detection of the planetary signal does not bias any other property of the lens star, such as its mass or distance. If there was a strong dependence of the planet hosting probability at the measured mass ratio of $9.3^{+0.2}_{-0.1} \times 10^{-3}$, then this implicit prior could lead to incorrect conclusions. Some theoretical papers based on core-accretion (Laughlin et al. 2004; Kennedy & Kenyon 2008) and observations of radial velocity (Johnson et al. 2010) have argued that gas giants are less frequent orbiting low-mass stars, however, this much of this difference disappears when the planets are classified by their mass ratio, q, instead of their mass. Nevertheless, since the host mass dependence of the planet hosting probability is not well measured, we investigate how our results depend on the choise of this prior.

We take the planet hosting probability for this event to take a power law form, $P_{\rm host} \propto M^{\alpha}$, and we have conducted Bayesian analyses with $\alpha = 1$, $\alpha = 2$ and $\alpha = 3$ in addition to the calculation with $\alpha = 0$, presented above. Figure 7 shows both the prior and posterior probability distributions for the lens mass, M_L, with these different values of α. The lens property values for each posterior distribution are shown in Table 5. The median of expected lens flux gets closer to the measured excess flux as α increases (i.e., the power law gets steeper), and consequently the median of the lens mass also gets higher and the parameter uncertainties get smaller. Thus, larger α values imply that more of the excess flux is likely to come from the lens. Nevertheless, our basic conclusion that the host is a M or K-dwarf hosting a gas giant planet remains for all of the $1 \leq \alpha \leq 3$ priors.

8. Discussion and Conclusion

We have analyzed the planetary microlensing event MOA-2016-BLG-227 which was discovered next to the field observed by the microlensing campaign (Campaign 9) of the *K2* Mission (Henderson et al. 2016). The event and planetary signal were discovered by the

MOA collaboration, but much of the planetary signal is covered by the Wise, UKIRT, CFHT and VST telescopes, which were observing the event as part of the *K2*C9 program. These data provide a unique microlensing light curve solution with a relatively large planetary mass-ratio of $q = 9.28^{+0.20}_{-0.11} \times 10^{-3}$. We considered several different extinction laws and decided that the N08 (Nishiyama et al. 2008) law was the best fit to our data, although our results would not change significantly with a different law. With this extinction law, we derive an angular Einstein radius of $\theta_E = 0.227^{+0.006}_{-0.009}$ mas, which yields the mass-distance relation given in Equation 2. We detected excess flux at the location of the source in a Keck AO image, and we performed a Bayesian analysis to estimate the relative probability of different sources of this excess flux, such as the lens, an ambient star, or a companion to the host or source (Koshimoto et al. 2017a). Our analysis excludes the possibility that the host star is a G-dwarf, leading us to a robust conclusion that the planet MOA-2016-BLG-227Lb is a super-Jupiter mass planet orbiting an M or K-dwarf star likely located in the Galactic bulge. Such systems are predicted to be rare by the core accretion theory of planet formation (Laughlin et al. 2004; Kennedy & Kenyon 2008). It is thought that such a planet orbiting at $a_{3d} \sim 2$ AU around a white dwarf host is unlikely (Batista et al. 2011).

Assuming the probability of a star hosting a planet does not depend on the host star mass or distance, our Bayesian analysis indicates the system consists of a host star with mass of $M_L = 0.29^{+0.23}_{-0.15} M_\odot$ orbited by a planet with mass of $M_{\rm p} = 2.8^{+2.2}_{-1.5} M_{\rm Jup}$ with a three-dimensional star-planet separation of $a_{3d} = 1.67^{+0.94}_{-0.35}$ AU. The system is located at $D_L = 6.5 \pm 1.0$ kpc from the Sun. We also considered different priors for the planet hosting probability as a function of mass. We use $P_{\rm host} \propto M^\alpha$ with $\alpha = 1, 2, 3$ as prior probabilities for the host star mass, in addition to the $\alpha = 0$ prior that we use for our main results. With larger α, the median value of the lens mass grows larger which results in a higher probability that large part of the excess -band flux comes from the lens. Johnson et al. (2010) found a linear (i.e., $\alpha = 1$) relationship between host mass and planet occurrence from 0.5 $M_\odot$ to 2.0 $M_\odot$ for giant planets within $\sim$ 2AU around hosts stars discovered by the radial velocity (RV) method. However, this analysis used a fixed minimum mass instead of a fixed mass ratio, and it does not appear that Johnson et al. (2010) did a detailed calculation of their detection efficiencies. Another result using RV planet data by Montet et al. (2014) gives $\alpha = 0.8^{+1.1}_{-0.9}$, using a sample more similar to the microlensing planets, i.e., gas giants orbiting at $0 < a < 20$ AU around M-dwarf stars. However, our basic conclusion that the MOA-2016-BLG-227L host star is an M or K-dwarf with a gas-giant planet located in the Galactic bulge would not change with a different α value, as indicated in Figure 6 and Table 5.

The probability that more than 90% of the excess flux seen in the Keck AO images comes from the lens is still 24.0% even assuming $\alpha = 0$. This is significant enough that we cannot ignore the possibility that most of the excess flux comes from the lens star. One approach

for obtaining further constraints is to get the color of the excess flux. If the excess flux is not from the lens, the derived lens mass and distance with $H_{\rm excess}$ may be inconsistent with the value derived using the excess flux in a different pass band, if we assume that all of the excess flux comes from the lens. However, such a measurement could also yield ambiguous results. Another, more definitive, approach is to observe this event in the future when we can expect to detect the lens-source separation through precise PSF modeling with high resolution space-based data (Bennett et al. 2007, 2015) or direct resolution with AO imaging (Batista et al. 2015). The lens-source relative proper motion value of $\mu_{\rm rel} = 4.88^{+0.14}_{-0.17}\,{\rm mas/yr}$ indicates that we can expect to be able to resolve the lens, if it provides a large fraction of the excess flux in ~ 2022 using *HST* (Bhattacharya et al. 2017) and in 2026 using Keck AO (Batista et al. 2015). Observations by the James Webb Space Telescope (Gardner et al. 2006), the Giant Magellan Telescope (Johns et al. 2012), the Thirty Meter Telescope (Nelson & Sanders 2008) and the Extremely Large Telescope (Gilmozzi & Spyromilio 2007) could detect the lens-source relative proper motion much sooner. If the separation of the excess flux from the source is different from the prediction of the microlensing model in these future high angular resolution observations, it would indicates that the lens is not the main cause of the excess flux, implying a lower mass planetary host star.

Work by N.K. is supported by JSPS KAKENHI Grant Number JP15J01676. The MOA project is supported by grants JSPS25103508 and 23340064. D.P.B., A.B., and D.S. were supported by NASA through grants NNX13AF64G, NNX16AC71G, and NNX16AN59G. Work by Y.S. and C.B.H. was supported by an appointment to the NASA Postdoctoral Program at the Jet Propulsion Laboratory, California Institute of Technology, administered by Universities Space Research Association through a contract with NASA. N.J.R. is a Royal Society of New Zealand Rutherford Discovery Fellow. Work by C.R. was supported by an appointment to the NASA Postdoctoral Program at the Goddard Space Flight Center, administered by USRA through a contract with NASA. Work by S.C.N. was supported by NExScI. A.C. acknowledges financial support from Université Pierre et Marie Curie under grants Émergence@Sorbonne Universités 2016 and Émergence-UPMC 2012. This work was supported by a NASA Keck PI Data Award, administered by the NASA Exoplanet Science Institute. Data presented herein were obtained at the W. M. Keck Observatory from telescope time allocated to the National Aeronautics and Space Administration through the agency's scientific partnership with the California Institute of Technology and the University of California. The Observatory was made possible by the generous financial support of the W. M. Keck Foundation. The authors wish to recognize and acknowledge the very significant cultural role and reverence that the summit of Mauna Kea has always had within the indigenous Hawaiian community. We are most fortunate to have the opportunity to conduct observations from this mountain. The United Kingdom Infrared Telescope (UKIRT)

is supported by NASA and operated under an agreement among the University of Hawaii, the University of Arizona, and Lockheed Martin Advanced Technology Center; operations are enabled through the cooperation of the Joint Astronomy Centre of the Science and Technology Facilities Council of the U.K. We acknowledge the support from NASA HQ for the UKIRT observations in connection with $K2C9$. This research uses data obtained through the Telescope Access Program (TAP), which has been funded by the National Astronomical Observatories of China, the Chinese Academy of Sciences (the Strategic Priority Research Program "The Emergence of Cosmological Structures" Grant No. XDB09000000), and the Special Fund for Astronomy from the Ministry of Finance. This work is partly based on observations obtained with MegaPrime/MegaCam, a joint project of CFHT and CEA/DAPNIA, at the Canada-France-Hawaii Telescope (CFHT) which is operated by the National Research Council (NRC) of Canada, the Institut National des Science de l'Univers of the Centre National de la Recherche Scientifique (CNRS) of France, and the University of Hawaii. This work was performed in part under contract with the California Institute of Technology (Caltech)/Jet Propulsion Laboratory (JPL) funded by NASA through the Sagan Fellowship Program executed by the NASA Exoplanet Science Institute. Work by MTP and BSG was supported by NASA grant NNX16AC62G. This work was partly supported by the National Science Foundation of China (Grant No. 11333003, 11390372 to SM). Based on observations made with ESO Telescopes at the La Silla Paranal Observatory under programme ID 097.C-0261.

A. Comparison of Different Extinction Laws

In Section 5.2, we obtained the observed extinction value, $A_{I,\rm obs} = 0.98 \pm 0.07$, and color excess values of $E(V-I)_{\rm obs} = 0.82 \pm 0.04$, $E(V-H)_{\rm obs} = 1.67 \pm 0.11$ and $E(I-H)_{\rm obs} = 0.81 \pm 0.07$. Then, we fit these values to the extinction laws of Cardelli et al. (1989), Nishiyama et al. (2009) and Nishiyama et al. (2008) separately and compared the results. This was motivated by the fact that Nataf et al. (2016) reported a clear difference of their extinction law towards the Galactic bulge from the standard law of Cardelli et al. (1989). Hereafter, we refer to these papers as C89, N09 and N08, respectively. Note that the four observed extinction parameters (1 extinction and 3 color excess) are not independent. They can be derived from the three independent extinction values: $A_{I,\rm obs}$, $A_{V,\rm obs}$ and $A_{H,\rm obs}$.

The C89 law is given by equations (1) - (3b) in their paper, and A_V and R_V serve as the parameters of their model.

Unlike C89, N09 does not provide a complete extinction model. They provide only ratios of extinctions for wavelengths longer than the J-band. So, we need additional information

relating A_V or A_I and A_J, A_H or A_K in order to calculate the values that we need for this paper: A_I, A_V and A_H. Therefore we used the $R_{JKVI} \equiv E(J-K_s)/E(V-I)$ values from Nataf et al. (2013) in addition to the N09 extinction law. The R_{JKVI} value at the nearest grid point to the MOA-2016-BLG-227 event in Table 3 of Nataf et al. (2013) is 0.3089. However the quality flag for this value is 1, which indicates an unreliable measurement, so we use a conservative uncertainty of $R_{JKVI} = 0.31 \pm 0.03$. We adjust A_I and $E(V-I)$ to minimize the χ^2 value between the observed $A_{I,\rm obs}$, $E(V-I)_{\rm obs}$, $E(V-H)_{\rm obs}$, and $E(I-H)_{\rm obs}$ values and those values derived using the ratio $A_{H,\rm 2MASS}/E(J-K_s)_{\rm 2MASS} = 0.89$ from N09, in conjunction with the R_{JKVI} value from Nataf et al. (2013). We explicitly use the $_{\rm 2MASS}$ subscript because N09 provides their result also in the IRSF/SIRIUS photometric system (Nagashima et al. 1999; Nagayama et al. 2003). Note that we calculate this $A_H/E(J-K_s)$ value using their result for the field S+ ($0^\circ < l < 3^\circ, -1^\circ < b < 0^\circ$), which is nearest of their fields to the MOA-2016-BLG-227 event position.

N08 also provide the ratio of extinctions towards the Galactic bulge ($l \sim 0^\circ, b \sim -2^\circ$). They find $A_J/A_V = 0.183 \pm 0.015$, $A_H/A_V = 0.103 \pm 0.008$ and $A_{K_s}/A_V = 0.064 \pm 0.005$. (These values are slightly different from the original values given by N08 because the values used in N08 were in the OGLE II and IRSF/SIRIUS photometric systems, so we converted them into the standard systems that we use here.) These values are well fit by a single power law, $A_\lambda/A_V \propto \lambda^{-2}$. Nevertheless, we use the ratios themselves, instead of the single power law, because N08 does not test that their power law accurately reproduces A_I/A_V, which we have now. As in the case of N09, we keep these ratios fixed, and adjust A_I and $E(V-I)$ to minimize the χ^2 between these relations and the observed $A_{I,\rm obs}$, $E(V-I)_{\rm obs}$, $E(V-H)_{\rm obs}$, and $E(I-H)_{\rm obs}$ values. Notice that N08 had V-band data and it was not necessary to use the R_{JKVI} as a constraint. Therefore we used the R_{JKVI} value as the additional observed data instead here in addition to $A_{I,\rm obs}$, $A_{V,\rm obs}$ and $A_{H,\rm obs}$ to increase the degrees of freedom (dof).

Table 6 shows the results of fitting our extinction measurements to these three different extinction laws. This table also shows the angular source radius calculated from the extinction–corrected source magnitudes and colors using formulae from the analysis of Boyajian et al. (2014). We determine $\theta_{*,IH}$ using Equations (1)-(2) and Table 1 of Boyajian et al. (2014), but the other relations were provided by private communications from Boyajian with a special analysis restricted to stellar colors that are relevant for the Galactic bulge sources observed in microlensing events. We use Equation (4) of Fukui et al. (2015) to determine $\theta_{*,VI}$, and we use Equation (4) of Bennett et al. (2015) to determine

$\theta_{*,VH}$. Those formulae are

$$\log\ [2\theta_{*,VI}/(1\mathrm{mas})] = 0.5014 + 0.4197(V-I)_{S,0} - 0.2I_{S,0}, \quad \text{(A1)}$$

$$\log\ [2\theta_{*,VH}/(1\mathrm{mas})] = 0.5367 + 0.0727(V-H)_{S,0} - 0.2H_{S,0}, \quad \text{(A2)}$$

$$\log\ [2\theta_{*,IH}/(1\mathrm{mas})] = 0.5303 + 0.3660(I-H)_{S,0} - 0.2I_{S,0}. \quad \text{(A3)}$$

If we compare the χ^2 value for each model fit in Table 6, we see that the χ^2/dof for the N09 and N08 laws are smaller than the value from the C89 extinction law, although the C89 is not disfavored by a statistically significant amount. (The p-value of $\chi^2 = 2.39$ for dof = 1 is still $\sim$0.12.) Note that a contribution of 0.96 to the total value of $\chi^2 = 1.19$ arises from fitting the R_{JKVI} value to the N08 extinction law. So, the remaining contribution of 0.23 to χ^2 arises from fitting the N08 model to our measurements of the RCG centroids. This indicates that the extinction law of N08 agrees with our measurement of the red clump centroids very well, but not quite so well with the R_{JKVI} value, which comes from Nataf et al. (2013).

From the point of view of consistency between the three θ_* values, the standard deviation of the three values (SD_{θ_*} in the table) is smallest using the N08 extinction laws. The N08 extinction law also yields the smallest error bars for A_H and $\theta_{*,VH}$.

Based on this analysis, we have decided to use the results from the N08 extinction laws in our analysis. We use $\theta_{*,VH}$ for the final angular source radius which is $\theta_* = 0.68 \pm 0.02\ \mu$as. We show the source magnitudes and colors corrected for extinction using the N08 extinction laws in Table 3.

REFERENCES

Alard, C. 2000, A&AS, 144, 363

Alard, C., & Lupton, R. H. 1998, ApJ, 503, 325

Alcock, C., Allsman, R. A., Alves, D., et al. 1995, ApJ, 454, L125

Batista, V., Gould, A., Dieters, S., et al. 2011, A&A, 529, A102

Batista, V., Beaulieu, J.-P., Gould, A., et al. 2014, ApJ, 780, 54

Batista, V., Beaulieu, J.-P., Bennett, D. P., et al. 2015, ApJ, 808, 170

Beaulieu, J.-P., Bennett, D. P., Batista, V., et al. 2016, ApJ, 824, 83

Beaulieu, J.-P., Bennett, D. P., Fouqué, P., et al. 2006, Nature, 439, 437

Bennett, D.P, 2008, in Exoplanets, Edited by John Mason. Berlin: Springer. ISBN: 978-3-540-74007-0, (arXiv:0902.1761)

Bennett, D. P. 2010, ApJ, 716, 1408

Bennett, D. P., Anderson, J., Bond, I. A., Udalski, A., & Gould, A. 2006, ApJ, 647, L171

Bennett, D.P., Anderson, J., & Gaudi, B.S. 2007, ApJ, 660, 781

Bennett, D. P., Batista, V., Bond, I. A., et al. 2014, ApJ, 785, 155

Bennett, D. P., Bhattacharya, A., Anderson, J., et al. 2015, ApJ, 808, 169

Bennett, D. P., Bond, I. A., Udalski, A., et al. 2008, ApJ, 684, 663

Bennett, D. P., & Rhie, S. H. 1996, ApJ, 472, 660

Bennett, D. P., Rhie, S. H., Nikolaev, S., et al. 2010, ApJ, 713, 837

Bennett, D.P., Rhie, S.H., Udalski, A., et al. 2016, AJ, 152, 125

Bensby, T., Yee, J. C., Feltzing, S., et al. 2013, A&A, 549, A147

Bertin, E., & Arnouts, S. 1996, A&AS, 117, 393

Bhattacharya, A., Bennett, D. P., Anderson, J., 2017, AJ, submitted (arXiv:1703.06947)

Bond, I. A., Abe, F., Dodd, R. J., et al. 2001, MNRAS, 327, 868

Bond, I. A., Bennett, D. P., Sumi, T., et al., 2017, MNRAS, submitted.

Bond, I. A., Udalski, A., Jaroszyński, M., et al. 2004, ApJ, 606, L155

Boulade, O., Charlot, X., Abbon, P., et al. 2003, Proc. SPIE, 4841, 72

Boyajian, T. S., van Belle, G., & von Braun, K. 2014, AJ, 147, 47

Bramich, D. M. 2008, MNRAS, 386, L77

Cardelli, J. A., Clayton, G. C., & Mathis, J. S. 1989, ApJ, 345, 245 (C89)

Carpenter, J. M. 2001, AJ, 121, 2851

Casagrande, L., & VandenBerg, D. A. 2014, MNRAS, 444, 392

Claret, A., & Bloemen, S. 2011, A&A, 529, A75

Duchêne, G., & Kraus, A. 2013, ARA&A, 51, 269

Fukui, A., Gould, A., Sumi, T., et al. 2015, ApJ, 809, 74

Gardner, J. P., Mather, J. C., Clampin, M., et al. 2006, Space Sci. Rev., 123, 485

Gaudi, B. S. 2012, ARA&A, 50, 411

Gaudi, B. S., Bennett, D. P., Udalski, A., et al. 2008, Science, 319, 927

Gilmozzi, R., & Spyromilio, J. 2007, The Messenger, 127, 11

Gonzalez, O. A., Rejkuba, M., Zoccali, M., et al. 2013, A&A, 552, A110

Gould, A. 1992, ApJ, 392, 442

Gould, A., & Loeb, A. 1992, ApJ, 396, 104

Gustafsson, B., Edvardsson, B., Eriksson, K., et al. 2008, A&A, 486, 951

Han, C., & Gould, A. 1995, ApJ, 447, 53

Henderson, C. B., Poleski, R., Penny, M., et al. 2016, PASP, 128, 124401

Hill, V., Lecureur, A., Gómez, A., et al. 2011, A&A, 534, A80

Johns, M., McCarthy, P., Raybould, K., et al. 2012, Proc. SPIE, 8444, 84441H

Johnson, J. A., Aller, K. M., Howard, A. W., & Crepp, J. R. 2010, PASP, 122, 905

Johnson, C. I., Rich, R. M., Kobayashi, C., Kunder, A., & Koch, A. 2014, AJ, 148, 67

Kennedy, G. M., & Kenyon, S. J. 2008, ApJ, 673, 502

Kervella, P., Thévenin, F., Di Folco, E., & Ségransan, D. 2004, A&A, 426, 297

Koshimoto, N., Bennett, D. P., et al. 2017a, in preparation.

Koshimoto, N., Udalski, A., Beaulieu, J. P., et al. 2017b, AJ, 153, 1

Koshimoto, N., Udalski, A., Sumi, T., et al. 2014, ApJ, 788, 128

Laughlin, G., Bodenheimer, P., & Adams, F. C. 2004, ApJ, 612, L73

Mao, S., & Paczynski, B. 1991, ApJ, 374, L37

Minniti, D., Lucas, P. W., Emerson, J. P., et al. 2010, New A, 15, 433

Montet, B. T., Crepp, J. R., Johnson, J. A., Howard, A. W., & Marcy, G. W. 2014, ApJ, 781, 28

Muraki, Y., Han, C., Bennett, D. P., et al. 2011, ApJ, 741, 22

Nagashima, C., Nagayama, T., Nakajima, Y., et al. 1999, Star Formation 1999, 397

Nagayama, T., Nagashima, C., Nakajima, Y., et al. 2003, Proc. SPIE, 4841, 459

Nataf, D. M., Gould, A., Fouqué, P., et al. 2013, ApJ, 769, 88

Nataf, D. M., Gonzalez, O. A., Casagrande, L., et al. 2016, MNRAS, 456, 2692

Nelson, J., & Sanders, G. H. 2008, Proc. SPIE, 7012, 70121A

Nishiyama, S., Nagata, T., Tamura, M., et al. 2008, ApJ, 680, 1174-1179 (N08)

Nishiyama, S., Tamura, M., Hatano, H., et al. 2009, ApJ, 696, 1407 (N09)

Sako, T., Sekiguchi, T., Sasaki, M., et al. 2008, Experimental Astronomy, 22, 51

Schechter, P. L., Mateo, M., & Saha, A. 1993, PASP, 105, 1342

Shvartzvald, Y., Bryden, G., Gould, A., et al. 2017, AJ, 153, 61

Shvartzvald, Y., Maoz, D., Kaspi, S., et al. 2014, MNRAS, 439, 604

Siverd, R. J., Beatty, T. G., Pepper, J., et al. 2012, ApJ, 761, 123

Spergel, D., Gehrels, N., Baltay, C., et al. 2015, arXiv:1503.03757

Sumi, T., Abe, F., Bond, I. A., et al. 2003, ApJ, 591, 204

Sumi, T., Kamiya, K., Bennett, D. P., et al. 2011 ApJ, 473, 349

Sumi, T., Udalski, A., Bennett, D. P., et al. 2016, ApJ, 825, 112

Szymański, M. K., Udalski, A., Soszyński, I., et al. 2011, Acta Astron., 61, 83

Tsapras, Y., Street, R., Horne, K., et al. 2009, Astronomische Nachrichten, 330, 4

Udalski, A. 2003, ApJ, 590, 284

Verde, L., Peiris, H. V., Spergel, D. N., et al. 2003, ApJS, 148, 195

Yee, J. C., Shvartzvald, Y., Gal-Yam, A., et al. 2012, ApJ, 755, 102

Yoo, J., DePoy, D. L., Gal-Yam, A., et al. 2004, ApJ, 603, 139

Zoccali, M., Renzini, A., Ortolani, S., et al. 2003, A&A, 399, 931

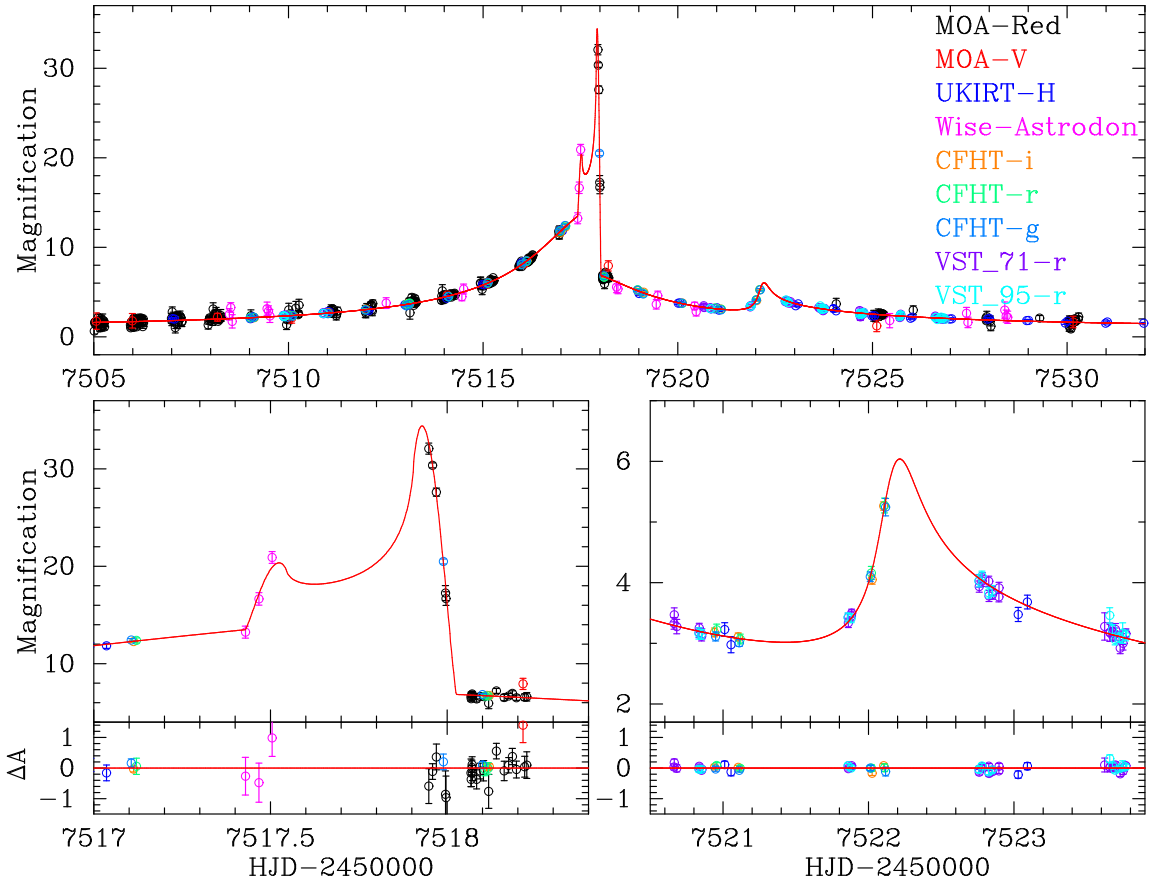

Fig. 1.— The light curve data for MOA-2016-BLG-227 is plotted with the best-fit model. The top panel shows the whole event, the bottom left and bottom right panels highlight the caustic crossing feature and the second bump due to the cusp approach, respectively. The residuals from the model are shown in the bottom insets of the bottom panels.

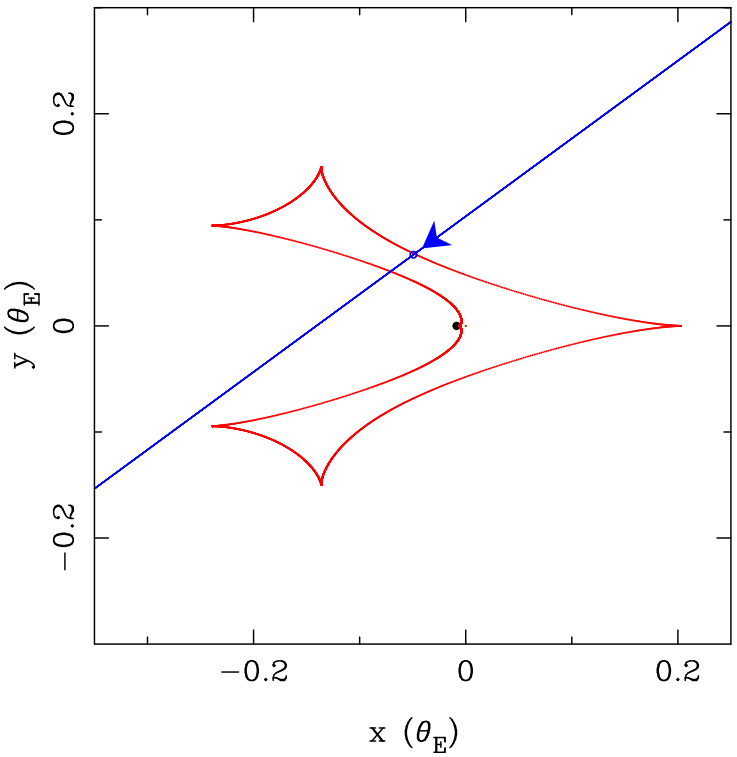

Fig. 2.— The caustic curve for the best-fit model. The blue arrowed line indicates the source trajectory and the tiny blue circle on the caustic entry indicates the source size.

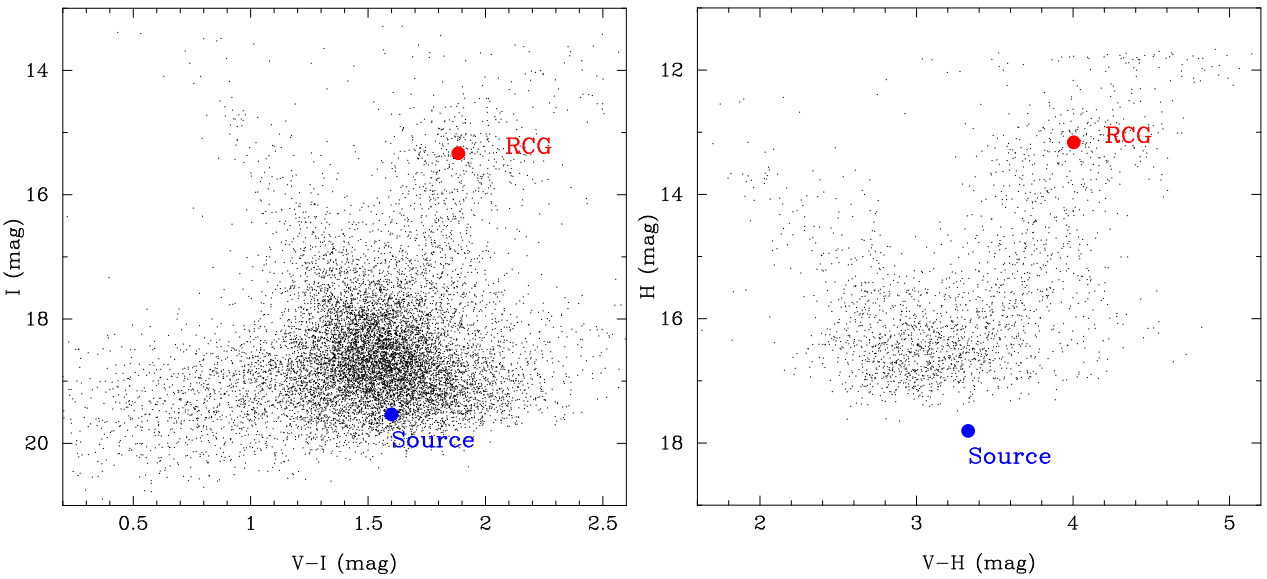

Fig. 3.— The color magnitude diagrams (CMDs) of stars within 2′ of the source star. The left panel shows $V-I$ vs I for the stars in OGLE-III catalog (Szymański et al. 2011), and the right panel shows $V-H$ vs H using stars from the OGLE-III catalog to the VVV catalog, which is calibrated to the 2MASS magnitude scale. The source star and the mean of red clump giants are shown as the blue and red dots, respectively.

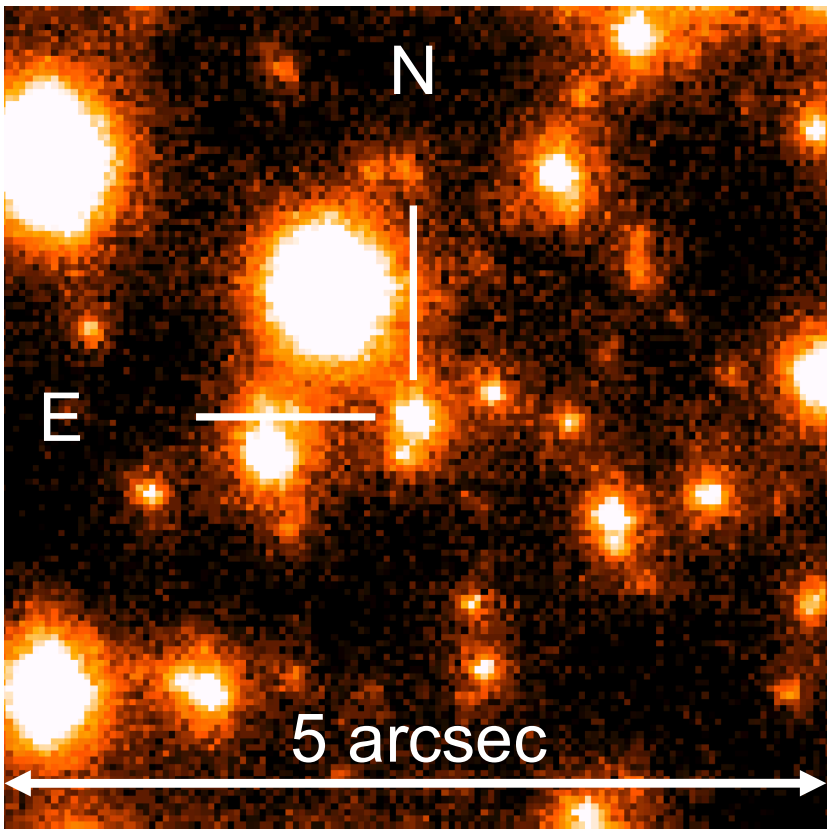

Fig. 4.— The co-added Keck II AO image of the event field. The target is indicated.

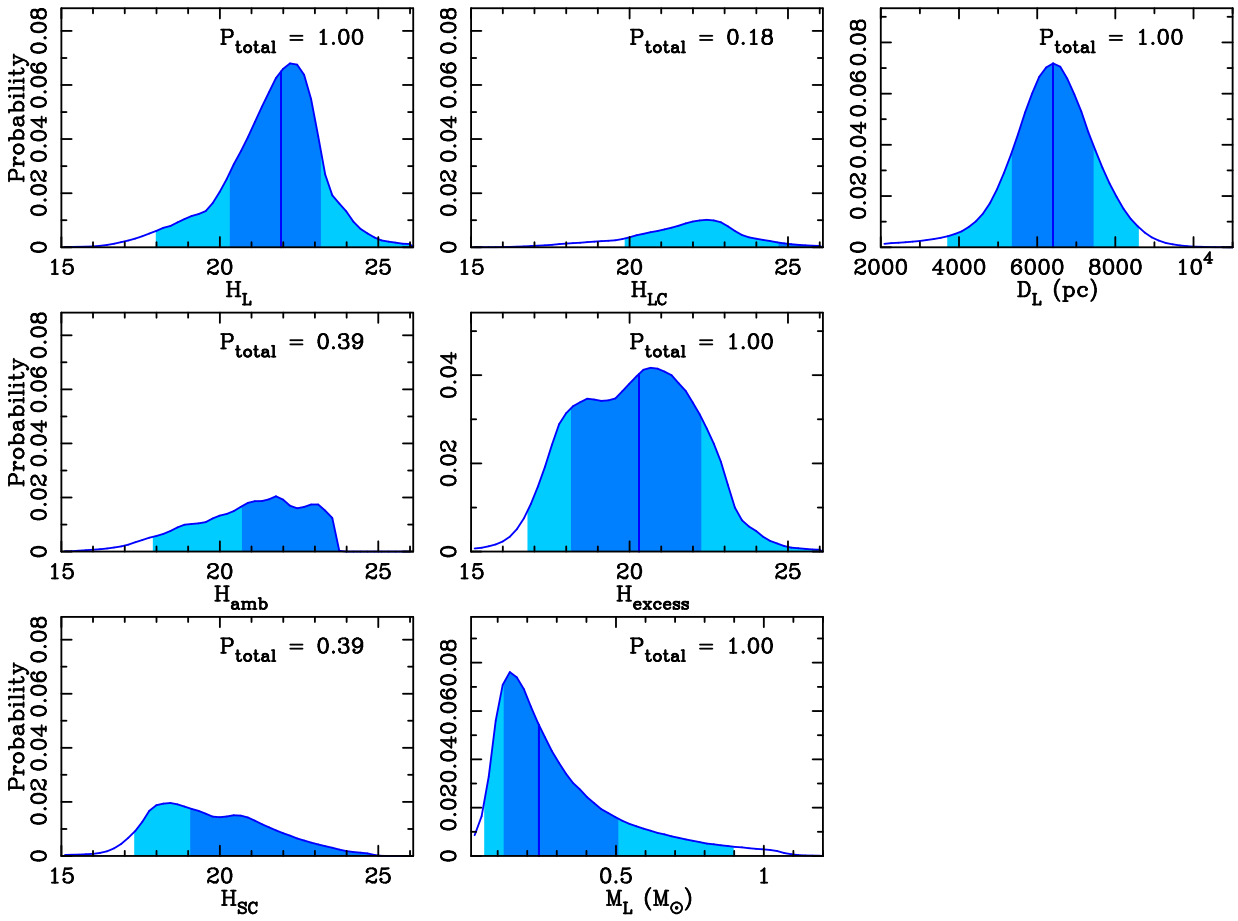

Fig. 5.— The prior probability distributions using the assumptions in Table 4 and light curve model constraints, as well as the seeing of the Keck AO image, but not the target flux. We assume that the planet hosting probability does not depend on the stellar mass. The borders between dark and light shaded regions indicate the 1σ limits and the borders between light shaded and white regions indicate 2σ limits. The $P_{\rm total}$ value in each panel is the probability that the object exists. The panels with $P_{\rm total} < 1$ indicate the probability that the companion or ambient star actually exists, and some of these do not have the borders of the $1\sigma/2\sigma$ limit within the plotted region.

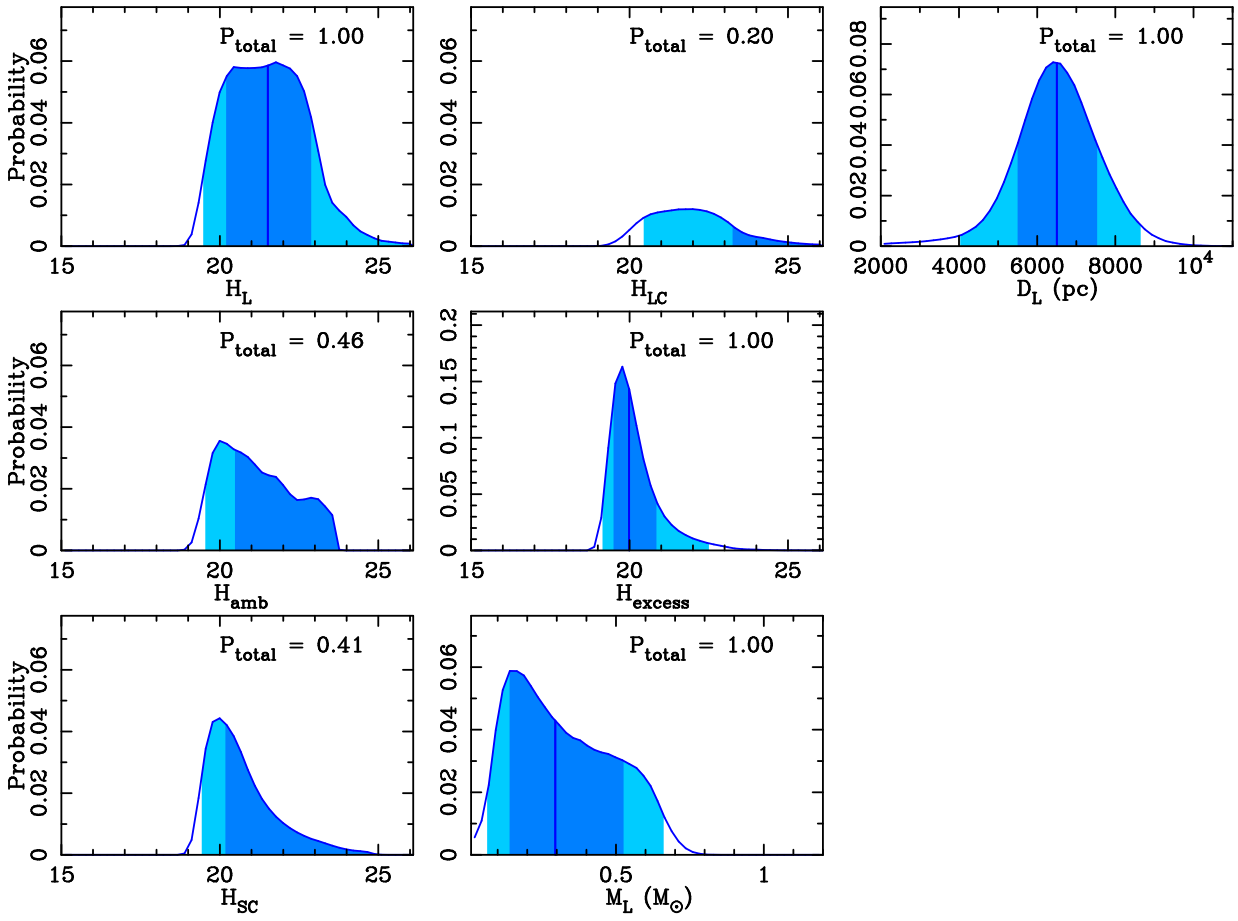

Fig. 6.— The posterior probability distributions generated by extracting combinations which have consistent excess flux values with $H_{\rm ex,obs} = 19.7 \pm 0.4$ (in flux unit) from the prior probability distributions in Figure 5.

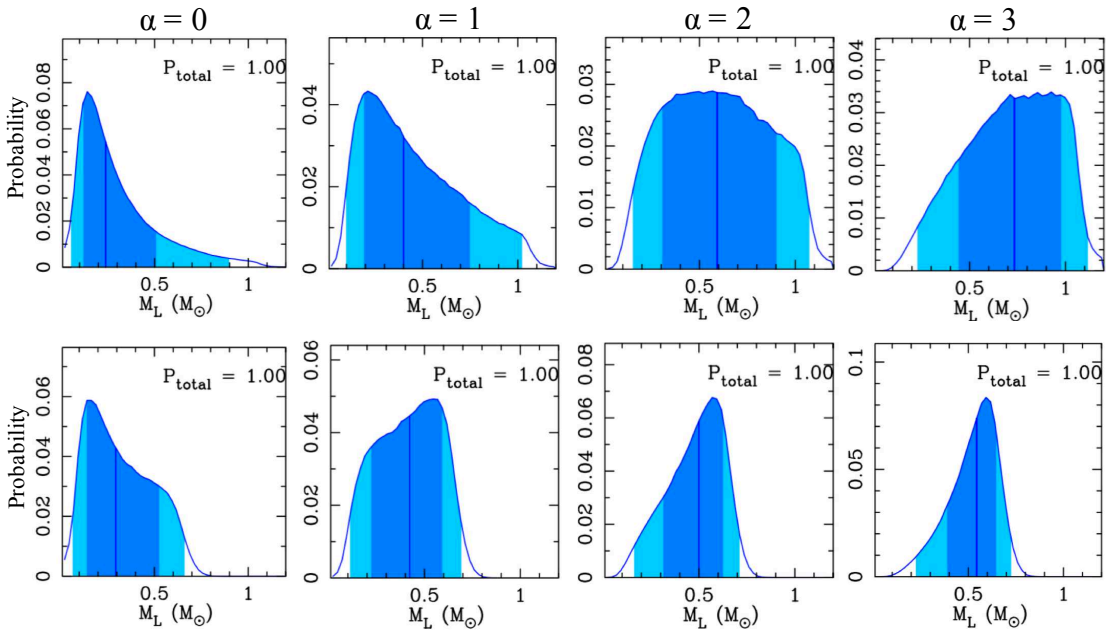

Fig. 7.— The prior (top) and posterior (bottom) probability distributions of the lens mass M_L using different priors for the planet hosting probability, which is assumed to follow a power law, $P_{\rm host} \propto M^{\alpha}$. The $\alpha = 0$ plots are repeated from Figures 5 and 6.

Table 1: The data and the parameters for the modeling.

Dataset	Number of data	k	$e_{\min}$	u_λ
MOA-Red[a]	1804	0.938	0	0.5585
MOA V	60	1.224	0	0.6822
Wise Astrodon[b]	44	1.267	0	0.6015[b]
UKIRT H	127	1.072	0.015	0.3170
CFHT i	77	1.673[c]	0.003	0.5360
CFHT r	77	3.028[c]	0	0.6257
CFHT g	78	2.105[c]	0	0.7565
VST-71 r[d]	193	1.018	0	0.6257
VST-95 r[d]	97	1.080	0	0.6257

Notes. Parameters k and $e_{\min}$ are used for the error normalization, and u_λ is the limb darkening coefficient.

[a] Approximately Cousins $R + I$.

[b] This filter blocks $\lambda < 500\,\mathrm{nm}$, and we use the limb darkening coefficient u_R to describe limb darkening in this filter.

[c] The CFHT error estimates were underestimated by a constant factor of 1.54, resulting in larger values of the k parameters.

[d] These use the same SDSS r filter, but different detectors, numbers 71 and 95, respectively.

Table 2: The parameters for the best-fit binary lens model.

Parameter	Unit	Value
t_0	HJD - 2450000	$7517.5078^{+0.007}_{-0.006}$
t_E	days	$17.03^{+0.08}_{-0.20}$
u_0	10^{-2}	$-8.33^{+0.08}_{-0.16}$
q	10^{-3}	$9.28^{+0.20}_{-0.11}$
s		$0.9312^{+0.0004}_{-0.0009}$
α	rad	$2.509^{+0.003}_{-0.004}$
ρ	10^{-3}	$3.01^{+0.09}_{-0.05}$
χ^2		2538.9
dof		2538

Notes. Superscripts and subscript indicates the the 84th and 16th percentile from the best-fit values, respectively.

Table 3: The source and RCGs magnitude and colors.

	I	$V-I$	$V-H$	$I-H$
RCG (measured from CMD)	15.33 ± 0.05	1.88 ± 0.02	4.03 ± 0.06	2.11 ± 0.03
RCG (intrinsic)	14.36 ± 0.05	1.06 ± 0.03	2.36 ± 0.09	1.30 ± 0.06
Source (measured from lightcurve)	19.54 ± 0.02	1.60 ± 0.03	3.33 ± 0.03	1.73 ± 0.02
Source (intrinsic) [a]	18.54 ± 0.09	0.78 ± 0.06	1.70 ± 0.11	0.92 ± 0.08

[a] Extinction corrected magnitudes using the Nishiyama et al. (2008) extinction model from Table 6

Table 4: Assumptions and undetectable limits used for the prior probability distributions

Priors of	Assumption	Closer limit	Wider limit	Used observed values
H_L	Galactic model	–	–	$t_{\rm E}$, $\theta_{\rm E}$
$H_{\rm amb}$	Luminosity function	–	0.8 FWHM	FWHM, Number density
H_{SC}	Binary distribution [a]	$\theta_E/4$	0.8 FWHM	FWHM, θ_E, H_S
H_{LC}	Binary distribution [a]	w_{LC}[b]$< u_0$	0.8 FWHM	FWHM, θ_E, u_0, M_L[c]

[a] The binary distribution used by Koshimoto et al. (2017a), based on Duchêne & Kraus (2013).
[b] The caustic size created by the hypothetical companion to the lens, $w_{LC} = 4q_{LC}/(s_{LC} - s_{LC}^{-1})^2$.
[c] The M_L value extracted from the prior probability distributions to calculate the H_L value.

Table 5: Lens properties calculated from the prior and posterior probability distributions.

Parameters	Unit	Prior $\alpha=0$	2σ range	Posterior $\alpha=0$	2σ range	Posterior $\alpha=1$	Posterior $\alpha=2$	Posterior $\alpha=3$
H_L	mag	$21.9^{+1.3}_{-1.6}$	18.0-28.7	$21.5^{+1.4}_{-1.3}$	19.5-27.5	$20.8^{+1.3}_{-0.9}$	$20.4^{+1.1}_{-0.7}$	$20.2^{+0.8}_{-0.6}$
M_L	$M_\odot$	$0.24^{+0.27}_{-0.12}$	0.06-0.90	$0.29^{+0.23}_{-0.15}$	0.07-0.66	$0.42^{+0.17}_{-0.20}$	$0.50^{+0.13}_{-0.18}$	$0.54^{+0.10}_{-0.15}$
$M_{\rm p}$	$M_{\rm Jup}$	$2.3^{+2.6}_{-1.2}$	0.5-8.8	$2.8^{+2.2}_{-1.5}$	0.6-6.4	$4.1^{+1.7}_{-1.9}$	$4.8^{+1.2}_{-1.8}$	$5.3^{+1.0}_{-1.5}$
D_L	kpc	6.4 ± 1.0	3.5-8.5	6.5 ± 1.0	3.9-8.6	$6.8^{+1.0}_{-0.9}$	$6.9^{+1.0}_{-0.9}$	$7.1^{+1.0}_{-0.9}$
$a_\perp$	AU	1.37 ± 0.23	0.76-1.84	1.39 ± 0.22	0.84-1.86	$1.45^{+0.22}_{-0.20}$	$1.49^{+0.22}_{-0.20}$	$1.51^{+0.22}_{-0.20}$
a_{3d}	AU	$1.64^{+0.93}_{-0.36}$	0.89-6.49	$1.67^{+0.94}_{-0.35}$	0.97-6.62	$1.74^{+0.99}_{-0.35}$	$1.79^{+1.02}_{-0.35}$	$1.82^{+1.03}_{-0.36}$
$P(f_L > 0.1)$[a]	%	72.2	-	78.1	-	90.8	96.5	98.7
$P(f_L > 0.5)$[a]	%	48.0	-	41.4	-	56.7	69.6	78.4
$P(f_L > 0.9)$[a]	%	33.8	-	24.0	-	29.9	38.0	44.5

Notes. The values of posterior probability distributions are shown also for different α values, the slope of the probability of hosting planets $P_{\rm host} \propto M^\alpha$. The values given in form of the median with the 1 σ uncertainty. The 2 σ range is given for $\alpha = 0$.

[a] The probabilities that the fraction of the lens flux to the excess flux, $f_L \equiv F_L/F_{\rm excess}$, is larger than the indicated values. The fractions of 0.1, 0.5 and 0.9 correspond to the difference of magnitude, $H_L - H_{\rm excess} = -2.5\ \log(F_L/F_{\rm excess})$, of 2.5 mag, 0.75 mag and 0.11 mag.

Table 6: Comparison of the extinction and angular Einstein radius based on different extinction laws.

Extinction law	None[a]	Cardelli et al. (1989)	Nishiyama et al. (2009)	Nishiyama et al. (2008)
Relation	-	$\frac{A_\lambda}{A_V} = a(x) + \frac{b(x)}{R_V}$ [b]	$\frac{A_H}{E(J-K_s)}$, R_{JKVI} [c]	$\frac{A_I}{A_V}$, $\frac{A_H}{A_V}$, $\frac{A_{K_s}}{A_V}$
A_V	1.80 ± 0.08	1.87 ± 0.12	1.83 ± 0.12	$\mathbf{1.82 \pm 0.12}$
A_I	0.98 ± 0.07	1.04 ± 0.10	1.01 ± 0.08	$\mathbf{1.00 \pm 0.08}$
A_H	0.17 ± 0.10	0.30 ± 0.04	0.23 ± 0.04	$\mathbf{0.19 \pm 0.02}$
$E(V-I)$	0.82 ± 0.04	0.83 ± 0.05	0.82 ± 0.05	$\mathbf{0.82 \pm 0.05}$
$E(V-H)$	1.67 ± 0.11	1.57 ± 0.10	1.60 ± 0.11	$\mathbf{1.63 \pm 0.11}$
$E(I-H)$	0.81 ± 0.07	0.73 ± 0.06	0.78 ± 0.09	$\mathbf{0.81 \pm 0.08}$
χ^2/dof [d]	-	2.39/1	0.56/1	1.19/2[e]
$\theta_{*,VI}$ (μas)	0.65 ± 0.04	0.67 ± 0.06	0.66 ± 0.05	0.66 ± 0.05
$\theta_{*,VH}$ (μas)	0.67 ± 0.04	0.73 ± 0.02	0.70 ± 0.02	$\mathbf{0.68 \pm 0.02}$
$\theta_{*,IH}$ (μas)	0.71 ± 0.07	0.79 ± 0.06	0.74 ± 0.06	0.72 ± 0.06
SD$_{\theta_*}$ [f]	0.035	0.061	0.042	0.030
$\theta_{\rm E}$ (mas) [g]	-	-	-	$\mathbf{0.227^{+0.006}_{-0.009}}$
$\mu_{\rm rel}$ (mas/yr) [g]	-	-	-	$\mathbf{4.88^{+0.14}_{-0.17}}$

Notes. The values in boldface are used as final values.

[a] Result without using an extinction law. The A_I, $E(V-I)$, $E(V-H)$ and $E(I-H)$ values are determined directly from the data.

[b] Equation (1) of C89, see the paper for the detailed model.

[c] The R_{JKVI} value comes from Table 3 of Nataf et al. (2013).

[d] When calculating the total χ^2, we multiply each of the contributions from $E(V-I)$, $E(V-H)$ and $E(I-H)$ by 2/3, because these values are not independent.

[e] The dof = 2 is because we used the R_{JKVI} value from Nataf et al. (2013) as an observed data point.

[f] Standard deviation of the three θ_* values.

[g] Calculations conducted only for the adopted θ_* value ($\theta_{*,VH}$ with N08).